Analysis of direct force measurements during capillary pinching of visco-elastic fluids in CaBER type experiments

JASPER VAN AEKEN[1], LUCA PASSARO[1], CHRISTIAN CLASEN[1]

[1]*Soft Matter, Rheology and Technology, Department of Chemical Engineering, KU Leuven, Celestijnenlaan 200F, Box 2424, BE 3001 Leuven, Belgium*

e-mail: christian.clasen@kuleuven.be

ORCID: 0000-0002-9253-9008

Abstract

A novel device is presented for direct measurement of the axial force evolution during the pinching of fluid filaments following an extensional step stretch, based on the 'tilted-CaBER'. The bending curve of the horizontally orientation fluid filament is fitted with the full expression of a catenary function, to directly and unambiguously extract the axial force from a single fitting parameter. The general limits of axial force determination from such devices are introduced in terms of a Bond number that accounts for the axial length scale.

The new set-up is validated using a Newtonian PDMS oil, for which the axial force scaling and the related prefactors X of the similarity solution are known. For dilute polymer solutions in form of a Boger fluid, the so far theoretical factor $X = 1.5$ for an Oldroyd-B model fluid could be experimentally approached for the first time with the new setup.

Key words

Horizontal CaBER; Capillary pinching; Capillary thinning; Force measurement; X-factor

Introduction

Extensional flow fields are abundantly present in nature as well as in industrial applications as for instance in inkjet printing, coating operations, electrospinning, etc. Henceforth, extensional flow fields have been the subject of extensive research over the past decades. (Cooper-White, Fagan, Tirtaatmadja, Lester, & Boger, 2002; Dirking, Willenbacher, & Boggs, 2001; Fong, Chun, & Reneker, 1999). In particular, low to medium viscous complex fluids such as automotive coatings and inks are very difficult to quantitatively understand. Due to the many versatile constituents of which the fluids are made up of, it is very difficult to predict the flow dynamics. In this respect, dissolved polymers are an often-encountered ingredient to control the viscoelastic properties of a fluids of interest. Polymer solutions have therefore regularly been employed to create model systems to study flow situations where viscoelasticity plays a dominant role in extension. (Clasen, 2010; Clasen, Phillips, Palangetic, & Vermant, 2011)

Several experimental techniques have been designed over the past decades to investigate the extensional flow behavior of complex fluids, where specifically the investigation of low viscosity solutions is challenging. (Hoath, 2016) Various home-built methods have been introduced. Opposed nozzle devices can achieve high extension rates, are easy in use and can control the strain rate. The device however has difficulties reaching a homogeneous flow, needs large sample volumes and always has a shear component in the flow field. (Dontula, Pasquali, Scriven, & Macosko, 1997; Fuller, Cathey, Hubbard, & Zebrowski, 1987) Another device is the four-roll mill which creates a quasi-homogeneous flow and works well for characterization when used together with optical techniques. But the device has difficulties in accurately calculating the extensional viscosity. (Dunlap & Leal, 1987; Lagnado & Leal, 1990; Taylor, 1934)

Commercially available techniques for investigating extensional properties of low viscosity solutions are the e-VROC extensional Viscometer and the capillary break-up extensional rheometer (CaBER). The e-VROC represents a viscosity indexer, as it provides an averaged viscosity value for an extensional flow through a hyperbolic contraction. (Ober, Haward, Pipe, Soulages, & McKinley, 2013) The CaBER on the other hand provides a more defined uniaxial extensional flow that allows the extraction of apparent extensional viscosities. In this device, a volume of fluid is placed between two circular plates to form a cylindrical filament. Subsequently, the plates are separated rapidly by a specified distance in order to create an

unstable liquid column which will pinch under the influence of capillary pressure. (Bazilevsky, Entov, & Rozhkov, 1990). While this decrease in diameter of the capillary bridge has been termed 'capillary thinning' in the past, we will relate to this in the following as capillary 'pinching'. This in order to avoid confusion with a deformation rate related loss of viscosity for which the term 'thinning' is commonly used (as for example in 'shear thinning'). The CaBER has the advantage that it only needs a small sample volume and that its experimental procedure is very straightforward. Moreover, it lends itself very well to measure lower viscosity solutions, very high strain rates can be achieved and a free surface flow is created which is very similar to processes like inkjet printing, spraying, … (Arnolds, Buggisch, Sachsenheimer, & Willenbacher, 2010) These characteristics make it an ideal technique to investigate low viscosity polymer solutions. (Clasen, Plog, et al., 2006; Cooper-White et al., 2002) An inexpensive variant of the CaBER with a less defined flow field has emerged recently with the dripping on substrate (DoS) protocol, that also creates and observes the pinching dynamics of a filament. (Dinic, Biagioli, & Sharma, 2017; Dinic, Jimenez, & Sharma, 2017)

From the pinching profile of the filament, parameters governing the extensional behavior can be extracted, such as the apparent extensional viscosity and the relaxation time. The idea to utilize this set-up as an extensional rheometer has been formulated already early on (Bousfield, Keunings, Marrucci, & Denn, 1986; Schümmer & Tebel, 1983). The bulk forces and stresses arising in a slender pinching filament are balanced with interfacial forces as surface and line tension, gravitational forces, inertial forces, and external traction. These bulk forces and stresses are usually obtained from solving the Navier-Stokes equation for an axisymmetric column of an incompressible fluid in a cylindrical coordinate system. Eggers and Dupont (Eggers & Dupont, 1994) as well as Garcia and Castellanos (García & Castellanos, 1994) showed in detail how this solution could be simplified by only retaining the lowest order terms of the radial expansions of velocities and the pressure entering the momentum balance, and of the normal and tangential stress boundary conditions. This leading order approximation of the momentum balance is given by equation 1.

$$\rho(\dot{v} + vv') = -\gamma\kappa' + D^{-2}[D^2(\sigma_{zz} - \sigma_{rr})]' \tag{1}$$

where D is the minimum diameter, $\kappa = \frac{4}{D\sqrt{4+D'^2}} - \frac{4D''}{(4+D'^2)^{3/2}}$ is the mean curvature of the axisymmetric surface of the filament, $\sigma_{zz} - \sigma_{rr}$ is the bulk normal stress difference, ρ is the

density, γ is the surface tension of the fluid and the dots denote temporal derivatives, $'$ and $''$ denote the first and second spatial derivative in the axial direction, respectively.

Integrating over the filament then yields the axial force balance and the axial tension F_z, for which at the cross-section of the minimum radius

$$\frac{4F_z}{\pi D^2} = \gamma K + (\sigma_{zz} - \sigma_{rr}) \tag{2}$$

It should be noted that this balance contains in principle on the right hand side also the radial inertial contribution $\frac{\rho}{16}\ddot{D}D$ as derived by Szabo (Mathues, Formenti, McIlroy, Harlen, & Clasen, 2018; Szabo, 1997; Tirtaatmadja, McKinley, & Cooper-White, 2006) (while axial acceleration terms at the minimum radius vanish). This contribution has been omitted by Eggers in his derivation of the momentum balance approximation. This omission of inertia is justified for the viscous fluids considered here, for which the radial inertial contribution is subdominant to the bulk stress difference.

For the following discussion it is important to notice that the surface tension term γK appearing in eq. 2 contains not only the Laplace pressure contribution arising from the mean curvature κ, but also the line tension contribution in the axial direction of the cylindrical coordinate system of the slender filament. (Clasen, Eggers, Fontelos, Li, & McKinley, 2006; Fontelos & Li, 2004; Li & Fontelos, 2003). This can be seen when rewriting the mean curvature gradient in the momentum balance to match the form of the bulk stress term (Entov & Yarin, 1984) as $\kappa' = -D^{-2}[D^2K]'$ where K can be written as

$$K = -\frac{4}{D\sqrt{4+D'^2}} + \frac{4D''}{(4+D'^2)^{3/2}} + \frac{8}{D\sqrt{4+D'^2}} \tag{3}$$

The first two terms on the RHS are just the negative mean curvature -κ, while the last term represents the line tension. Since the line tension and the first term of the mean curvature have the same form except for a factor -2, they are usually combined to give $K = \frac{4}{D\sqrt{4+D'^2}} + \frac{4D''}{(4+D'^2)^{3/2}}$ (Clasen, Eggers, et al., 2006). This form looks very similar to the mean curvature definition, except for the sign change of the first term, which has led to some confusion in the past as well as the neglection of the line tension and the axial tension. The line and axial tension are, however, crucial for the correct determination of material parameters in the following (see also the appendix A in Bhat et al. (Bhat, Appathurai, Harris, & Basaran, 2012) for a clear

representation of this issue). For slender filaments, the mean curvature and line tension can then safely be reduced in eq. 2 to the leading order contributions of mean curvature and line tension $\gamma K \approx -2\gamma/D + 4\gamma/D = 2\gamma/D$.

Generally the axial tension F_z cannot simply be reduced to the bulk stress contribution as surface and line tension contributions can be of similar order of magnitude as the bulk stresses. (Bhat et al., 2012). The total axial tension F_z is in principle not known a priori, and depends on the fluid properties and the resulting shape of the filament connecting the two end droplets. This initially prevented the use of the experimentally observed pinching rate

$$\dot{\varepsilon} = -\frac{2\dot{D}}{D} \tag{4}$$

to extract quantitatively fluid properties form the bulk stress difference as for example an apparent extensional viscosity (Schümmer & Tebel, 1983) in case F_z is not known:

$$\eta_E = \frac{\sigma_{zz} - \sigma_{rr}}{\dot{\varepsilon}} = \frac{4\,F_z/\pi D^2 - 2\gamma/D}{-2\dot{D}/D} \tag{5}$$

A first step to remediate this problem was set by McKinley and Tripathi (McKinley & Tripathi, 2000) who postulated that for a cylindrical Newtonian filament, the pressure of the mean curvature in eq. 2 is balanced by the (viscous) bulk stresses, $2\gamma/D = \sigma_{zz} - \sigma_{rr}$, so that the axial tension is equal to just the line tension contribution, $4F_z/\pi D^2 = 4\gamma/D$, and thus decays with the radius. They furthermore determined the axial tension, using eq. 2, from the actual pinching dynamics of a Newtonian fluid of viscosity η_S and a therefore known extensional viscosity $\eta_E = 3\eta_S$. The results were confirmed both by numerical simulations and experiments. They observed that for a real (non-cylindrical but slender) filament shape of the Newtonian liquid, the force F_z is just a fraction X of the line tension for the cylindrical case, but still decaying with the filament radius:

$$X = \frac{4F_z/\pi D^2}{4\gamma/D} = \frac{F_z}{\pi\gamma D} \tag{6}$$

Replacing the force in eq. 5 with this slightly reduced line tension $4F_z/\pi D^2 = 4X\gamma/D$ gives $\eta_E = (2X-1)\frac{\gamma}{-\dot{D}}$. The minimum filament radius of a Newtonian liquid decays linearly with time t in this visco-capillary (VC) balance regime as

$$D(t) = D_0 - (2X-1)\frac{\gamma}{3\eta_S}t \tag{7}$$

resulting also in an extension rate increasing with time following eq. 4. The observed magnitude of the front factor $X = 0.7127$ (or $(2X-1)/3 = 0.1418$), arises from the fluid property depending deviation of the slender filament shape from the perfect cylinder shape. This deviation is a consequence of an effectively lower resistance of the viscous stresses of the fluid against the capillary pressure. For a perfect cylinder the viscous stresses just balance the pressure arising from mean curvature κ (first two RHS terms in eq. 3) so that only line tension contributes to the axial tension and $X = 1$. For the theoretical case of an incompressible inviscid fluid with no resistance from the bulk, the axial tension would arise from line tension reduced by the full capillary pressure, so that $X = 0.5$. The observed $X = 0.7127$ agrees indeed well with one of the similarity solutions that Papageorgiou derived theoretically for the self-similar shape of a pinching Newtonian filament connected to two end droplets (Papageorgiou, 1995).

For other fluid properties dominating the bulk stress, or inertial contributions to the force balance, the filament shape changes and different evolutions of the axial tension in the filament have been theoretically predicted. (Brenner, Lister, & Stone, 1996; Clasen, Eggers, et al., 2006; Eggers, 1993, 1997; Papageorgiou, 1995) Eggers predicted that, with decreasing filament diameter, inertia of the fluid accelerating in the filament will eventually balance viscous forces. Also within this inertial-viscous (IV) balance, regime the axial tension decays with the diameter so that still a linear decay of the minimum radius following eq. 7 is observed. The axial tension however has a different factor $X = 0.5912$ (or $(2X-1)/3 = 0.0608$) as follows from Eggers' universal similarity solution of the IV regime (Eggers, 1993, 1997). The transition to a lower pinching rate that is obtained when inserting this theoretical lower X-factor into eq. 7 has also been confirmed experimentally. (Lang et al., 2019; Mathues et al., 2018; Verbeke et al., 2020)

Clasen et al. derived theoretically that for a viscoelastic liquid that can be represented by an Oldroyd-B type model with a single relaxation time, the axial tension is again proportional to the minimum radius of the, in this case, near cylindrical filament. An asymptotical analysis in the center of the thread and a similarity analysis in the corner region where the filament is attached to the end droplet showed that the bulk stress is dominated by the elastic contribution arising from the Oldroyd-B model. These exponentially increasing elastic bulk stresses turned out to be with $4\gamma/D = \sigma_{zz} - \sigma_{rr}$ a factor 2 larger than the viscous bulk stresses for the Newtonian cylindrical filament, resulting therefore in larger factor $X = 1.5$ (or $(2X-1)/3 = 2/3$) (Clasen, Eggers, et al., 2006). Bhat et al. (Bhat et al., 2012) later completed the similarity

solution for this case by including the capillary pressure effect in the end drops for early thinning stages, where this effect is not subdominant to pressure within the filament as assumed by Clasen et al.

Entov and Hinch had demonstrated that, for a discrete spectrum of relaxation times as in a Zimm spectrum, the stretch rate in the pinching filament will excite only the longest mode. This means that the Oldroyd-B approach with a single relaxation can be readily applied to fluids exhibiting a Zimm spectrum as dilute polymer solutions (Bousfield et al., 1986; Entov & Hinch, 1997). Outgoing from this model and the related axial tension, the filament radius in this elasto-capillary (EC) balance regime decays exponentially with time (Clasen, Eggers, et al., 2006; Mathues et al., 2018)

$$D(t) = \left(\frac{GD_0^4}{16\gamma}\right)^{\frac{1}{3}} \exp\left(-\frac{t}{3\lambda_e}\right) \tag{8}$$

where G is the elastic modulus and λ_e is the longest extensional relaxation time of the Zimm spectrum. The pinching rate is in this case constant and set by this longest relaxation time of the unraveling polymer chain $\dot{\varepsilon} = -\frac{2\dot{D}}{D} = \frac{2}{3\lambda_e}$. Inserting this expression for the strain rate and the expression of the axial tension F_z of eq. 6 for X= 1.5 into eq. 5 gives an extensional viscosity evolution $\eta_E = \frac{6\gamma\lambda_e}{D}$ inversely proportional to the filament diameter.

A downside of the approach to calculate material properties from the scaling relations of equations 7 and 8 is that they rely on the assumption that the applicable scaling law is clearly identifiable and sufficiently dominating. This needs to occur in such a way that only this specific relation and the related axial force evolution are applicable. However, within the transition zones between the different scaling regimes the axial force evolution is not well defined, and the transition zones can be so stretched out that they overlay to the point that they obscure the single scaling laws (Clasen, Plog, et al., 2006).

In order to evaluate which material parameters can be extracted from the pinching dynamics of the capillary bridge, it has to be known a priori which material property is predominantly resisting the capillary action. With this knowledge, it is feasible to fit the data with the appropriate constitutive model, a catch-22 for an unknown fluid. A possible route to solve this is with the observation of the silhouette of the pinching capillary bridge. As for example

summarized in an earlier review of McKinley (McKinley, 2005), Newtonian, power-law, weakly-elastic and elastic fluids or Bingham plastics each have their specific shape of the pinching capillary bridge. This filament shape can be utilized to identify the dominating material property. A recent overview of such shapes for a variety of material classes can be found in the work of Dinic (Dinic, Jimenez, et al., 2017).

Similarly, the scaling of the decay of the minimum radius of the pinching bridge with time described above can be used to identify the dominant resisting material properties. Linear, exponential or logarithmic radii decays have respectively been linked for example to Newtonian, extension thinning, or elastic material responses. However, both approaches are not unambiguous, as for example the capillary bridge shapes of a yielding Bingham plastic and an extension thinning power law fluid are nearly indistinguishable. Also, a linear radius decay is observed for both a viscous as well as an inertial-viscous resistance. Furthermore, a single scaling regime is observable in only a few cases. Early times are often overlaid by gravitational drainage or inertial flows, and late times show transitions to again an inertial regime (Eggers, 1997) or the approach to finite extensibility of elastic structures. This requires the *a priori* knowledge that a specific decay regime is expected, in order to identify this in the complex liquid bridge decay pattern.

Other approaches use a non-dimensional analysis to determine the presence of a material property's dominance in the extensional flow of the pinching capillary bridge. The calculation of the Ohnesorge, elasto-capillary, or intrinsic Deborah number, based on the geometrical parameters of the bridge as the characteristic length scales, allows to determine the eventual presence of an inertial, viscous or elastic controlled pinching (Clasen, 2010; Clasen et al., 2011). Still, this approach for the non-dimensional number calculation usually utilizes parameters as viscosities or relaxation times often obtained from shear experiments. These parameters are not directly transferable to the extensional flow for non-linear material responses and give in this case only qualitative predictions of observable regimes.

It is thus highly desirable to be able to measure the axial force and its decay over the whole course of the filament pinching process. This would support the identification of the present scaling regimes by comparison to the theoretically predicted forces from equation 6 and the respective X-factors. This would in particular be helpful to determine the absolute fluid stress

component $\sigma_{zz} - \sigma_{rr}$ in equation 5 to reflect the apparent extensional viscosity evolution correctly over the whole pinching process, and thus also within the transitional zones. To achieve this, Klein et al. implemented a force transducer into the endplate of a commercially available CaBER device (Haake). Forces were measurable down to 50 µN, however, the strong initial stresses prevented the applicability to the small forces encountered during the later stages of capillary pinching in the CaBER (Klein, Naue, Nijman, & Wilhelm, 2009). Furthermore, the positioning of the sensor in the endplate resulted in the inevitable presence of gravitational forces from the remaining fluid droplets that the pinching filament connects, which tend to obscure the relatively small axial forces arising in the filament.

Recently, Sachsenheimer et al. have demonstrated that, by executing a CaBER experiment horizontally, the axial force can be derived from the bending of the filament under gravity. The horizontal method showed good results in agreement with the postulated X-factor of 0.7127 by McKinley and Tripathi for purely viscous fluids. (McKinley & Tripathi, 2000) The technique has further been applied to investigate semi-dilute and concentrated polymer solutions as well as wormlike micellar solutions. (Sachsenheimer, Hochstein, Buggisch, & Willenbacher, 2012; Sachsenheimer, Hochstein, & Willenbacher, 2014)

The promising approach of the horizontal CaBER technique has not yet been quantitatively applied and tested for the full range of fluids and scaling laws available in literature.

We present in this paper a home-built device constructed based on the principles of CaBER. The novel device allows the observation of horizontal filament pinching following Sachsenheimer et al. (Sachsenheimer et al., 2012). The motion of the top plate can be finely tuned to attenuate inertia effects as much as possible and extend the measurable range in horizontal orientation down to around 20 mPa·s, which allows to access the pinching dynamics even of low viscosity fluids. Furthermore, a general window of operation in terms of the diameter is established in which measurements can be determined trustworthy.

The paper is structured as follows. ‘Materials & Methods’ gives a short overview of the fluids and polymers used, together with construction data of the home-built rheometer. Furthermore, a rigorous way to analyze the filament shape and to determine stresses quantitatively is described. A window of operation, in terms of an adapted definition of the Bond number, is

presented in which experiments can be deemed trustworthy. 'Results and discussion' shows then the validation of the instrument and its results of horizontal stretching using a Newtonian fluid. Subsequently, the so far only theoretically postulated similarity solutions of the pinching process for dilute polymer solutions evaluated. Finally, low viscosity dilute and semi-dilute polymer solution are tested to map the limitations of the new device in terms of the measurable viscosity range. 'Conclusion' summarizes the main findings extracted from the measurements.

Materials and methods

Materials

Six liquids have been used to probe the new apparatus, of which the main parameters are presented in Table 1:

- PDMS 5 Pa·s
- PIB Boger solution: 0.2 wt% Oppanol B200 in PIB Infineum S1054
- Dilute PS solution: 0.1 wt% PS6M in DEP
- Semi-dilute PS solution: 0.5 wt% PS6M in DEP
- Semi-dilute PEO solution: 0.06 wt% PEO8M in 40 wt% PEO35k-in-water solution

Table 1 Main properties of used fluids at 22°C

Fluid	$\eta_0\ [Pa \cdot s]$	$\gamma\ \left[\frac{mN}{m}\right]$	$\rho\ \left[\frac{kg}{m^3}\right]$	$\frac{c}{c^*}\ [-]$
PDMS 5	5.9	21.4	965	NA
PIB Boger fluid	54.9	26.0	935	/
0.1 wt% PS6M in DEP	$2.15 \cdot 10^{-2}$	35.4	1099.1	0.59
0.5 wt% PS6Min DEP	0.5	35.4	1099.1	2.94
0.06 wt% PEO8M in 40 wt% PEO35k in H_2O	0.2	57.6	1080	1.72

PDMS (Bluesil FLD 47 V5.000) has been used as received. The PIB Boger fluid (Boger, 1977) is prepared by dissolving 0.2 wt% Oppanol B200 (M_w = 4.1·10^6 g/mol) in PIB Infineum S1054. Ingredient sources, preparation and other characteristics than those given in Table 1 of this Boger fluid can be found in the work of Verhulst, where the fluid is referred to as 'BF2'. (Verhulst, Moldenaers, & Minale, 2007) The overlap concentration is not determined exactly.

The rheological behavior of this solution as a Boger fluid is described in the work of Verhulst et al in detail.

Solutions of polystyrene (PS; Polymer Standards Service: PSS-ps6.5m; M_w = 6.5·10^6 g/mol) in diethyl phthalate (DEP; Sigma-Aldrich (Merck)) are prepared by weighing the required amount of PS on a Sartorius CPA225D balance and transferring it into a 20 ml glass vial. DEP is later added with a pipet after which the solution is put on a Heidolph Promax 2020 shaker at 150 rpm to ensure gentle dissolution. Mixing occurred for a minimum of 24 hours and continued until the solution was optically transparent. Two solutions of PS6M in DEP are prepared following a similar procedure, one in the dilute regime, and one in the semi-dilute. The overlap concentration is determined via the Graessley equation (Graessley, 1980)

$$c^* = \frac{0.77}{[\eta]} \tag{9}$$

where c^* is the overlap concentration and $[\eta]$ is the intrinsic viscosity. The intrinsic viscosity is determined with the Mark-Houwink equation (Rubinstein & Colby, 2003)

$$[\eta] = K M_w^a \tag{10}$$

where M_w is the molecular weight of the polymer and the parameters K and a for PS in DEP are extracted from Clasen et al. (Clasen, Plog, et al., 2006) With this the overlap concentration for PS6M in DEP is equal to 0.17 wt%. The dilute solution of 0.1 wt% is thus at 0.59 c^*, whereas the semi-dilute is at 2.94 c^* around three times the overlap concentration.

Another semi-dilute polymer solution based on PEO in water is prepared analogous to the work of Sankaran et al. (Sankaran, Dros, Meerman, Picken, & Kreutzer, 2013) The long chains of PEO (M_w = 8·10^6 g/mol) are obtained from Sigma-Aldrich (Merck), the shorter chains of PEG (M_w = 35.000 g/mol) are obtained from Fluka.

Figure 1 shows the flow sweep measurements for the varying fluids employed in this study, visible in Table 1. The flow sweeps were conducted in the range from 0.01 to 100 s^{-1}. The experiments were performed with a TA Instruments AR-G2 rheometer using a 60 mm cone with an angle of 1°. The zero-shear viscosity for the Newtonian PDMS is used for the validation of the instrument.

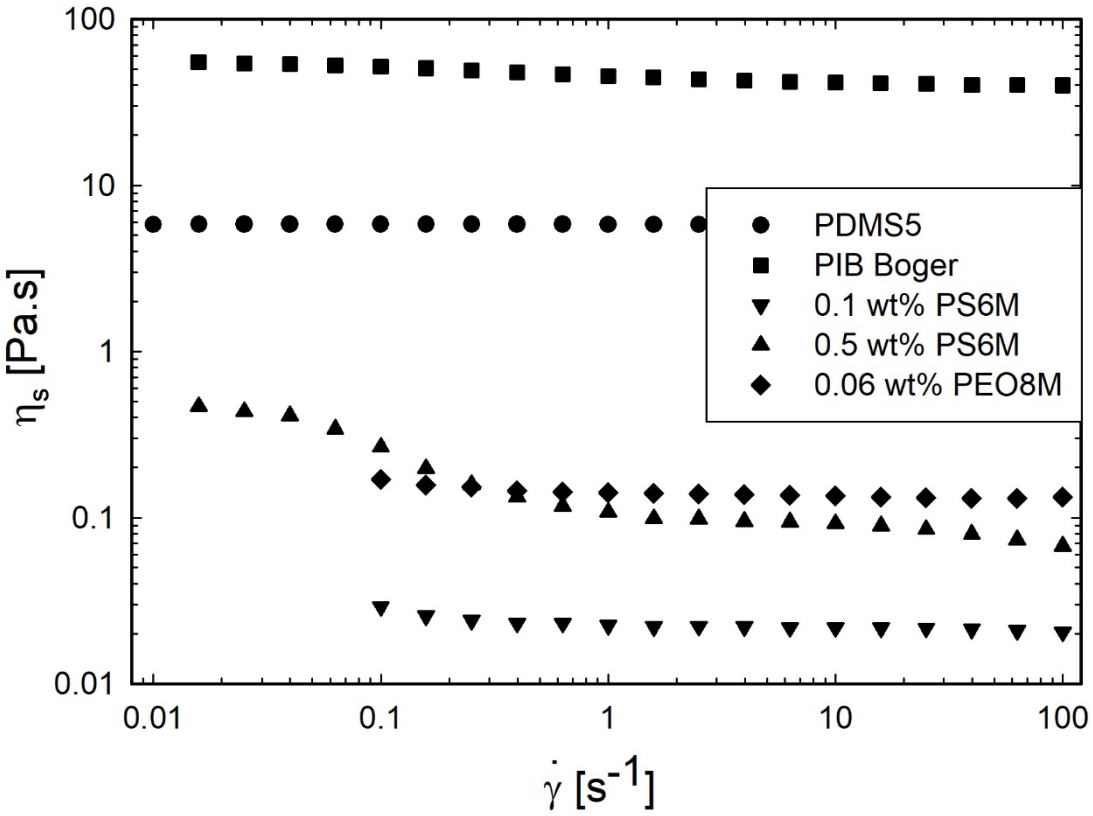

Fig. 1 Flow sweeps for all fluids measured in this study (see table 1).

New set-up

The new device to measure the pinching dynamics of liquid filaments is shown in figure 2. The set-up combines multiple functionalities with the possibility to precisely control temperature, conduct experiments in a liquid-in-liquid environment, and conduct vertical as well as horizontal pinching experiments. Figure 2a shows the entire set-up while figure 2b depicts a zoomed-in part of the fluid bath in the center.

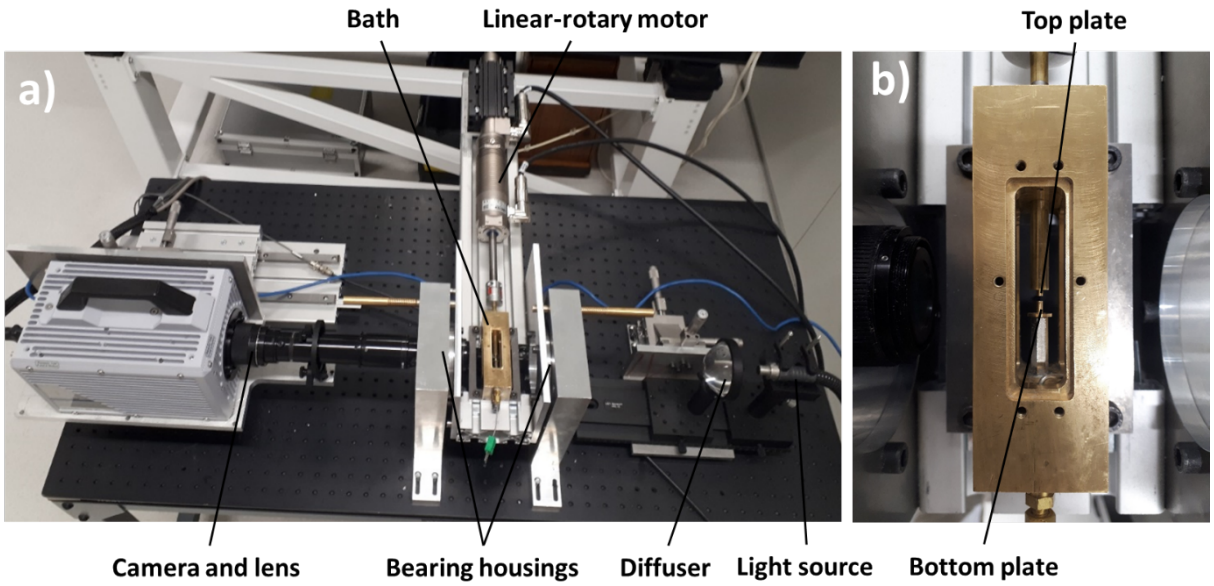

Fig. 2 a) Experimental set-up in horizontal orientation; b) Close-up of fluid 'bath' where windows are not attached

As can be seen on figure 2a, two large bearing housings hold a horizontal beam to which a brass fluid bath and a motor (LinMot PR01-52x60-R/37x120F-HP-C-100) are mounted, of which the latter can apply rotational as well as linear motion. The linear motion profile can freely be programmed, in particular with the possibility of a long deceleration step as to attenuate inertial effects as much as possible. Rotational motion can be applied in case preshear is of interest for the sample as for instance demonstrated previously for the study of wormlike micelle solutions. (Bhardwaj, Miller, & Rothstein, 2007)

The shaft of the motor is connected via a flexible coupling to a cylindrical rod which enters the fluid bath and holds the top plate in position. Plates with a diameter of 2 millimeters were used for the current experiments, with plates of 4 and 6 millimeters being available as well. The cell is optically accessible with a light path through the holes of the large bearings. The set-up allows to switch easily between horizontal to vertical orientation of the filament. A high speed camera (Photron FastCam SA2; 2048 x 2048 pixels, frame rate up to 86,400 frames per second) with a magnification lens (Navitar 12x Zoom, resulting in a square pixel resolution of 6.2 $\mu m^2/px$) is mounted on the left side (figure 2a), while on the right side a light source (Fiber-Lite DC-950) combined with a plano-convex collimator lens assembly (ThorLabs LMR75/M) is placed to create a telecentric illumination which is required to accurately determine the fluid filament silhouette.

Figure 2b shows the fluid bath. Windows can be mounted on all 4 sides to create a fluid reservoir to perform experiments with an inner and outer fluid. A plug-in connection is provided at the bottom of the bath to easily fill the bath up with a syringe pump. This set-up is advantageous for e.g. very volatile solutions (Sousa, Vega, Sousa, Montanero, & Alves, 2017) and to set up liquid-liquid experiments more accurately. (Verbeke et al., 2020) Furthermore, in the fluid bath cartridge heaters (Omega HDC19113) are inserted in holes in the corners of the brass frame for accurate temperature control via a RS Pro Type K thermocouple and a Red Lion PAX 2C controller.

For all samples, besides the Boger fluid, the fluid was filled with a 1 ml syringe with precision tip (Precision Tips: 7018336) between top and bottom plate which were spaced 0.5 mm. The Boger fluid was more difficult to load due to its high viscosity and elasticity. For this reason, a larger precision tip (Precision Tips: 7018333) was used and the initial spacing between the two plates was set at 1.5 mm to accommodate the larger tip. The gap was underfilled with the fluid, and the upper plate was subsequently lowered until a correct filling is acquired. Miller et al. have shown that the initial and/or final step height for purely viscous and dilute polymer solutions is not of importance, whereas the final step height does matter for semi-dilute polymer solutions. (Hendricks, 2019; Miller, Clasen, & Rothstein, 2009)

All experiments are conducted with small plates with a diameter of 2 mm to decrease effects of gravitational sagging. The moving plate translates a distance of 6 mm in a strike time between 20 and 100 ms. The longer strike times of 100 ms are chosen for the low viscous liquids to minimize the oscillations of the end droplets caused by the sudden de-acceleration of the endplates at the end of the strike (it should be noted that these strike times are still faster than the Rayleigh or visco-capillary timescales of the fluids, so that clearly observable filaments are formed). High viscous fluids such as the PIB Boger fluid for which the end droplet oscillations are sufficiently damped can be stretched faster at a strike time of 40 ms. All experiments were executed at an ambient temperature of 22°C. The frame rates of the video-imaging are adjusted to the duration of the experiments, to produce around 150-200 frames per pinching profile. Frame rates thus vary from 1 fps for the highly viscoelastic PIB Boger fluid to 2000 fps for the low visco-elastic PS-in-DEP solution.

Image analysis of bending filaments

In the horizontal orientation, the filament will bend under the influence of gravity. From the bending shape of the filament (once it has acquired this shape after the initial step stretch and the force balance holds), the axial tension force in the filament can be determined. For this the video-images obtained of the horizontal, bending filaments were processed with the self-written, Matlab-based image processing algorithm EdgeHog developed (Vadillo, Mathues, & Clasen, 2012) in order to determine the horizontal position of the upper and lower edge of the filament. The bending line of the filament is then obtained as the middle line between these two edges. From the now known shape and bending line of the hanging filament depicted in figure 3, and a known dependency of the shape on the axial tension force, the bending line can be fitted in order to extract the tension force and its evolution over the course of the filament pinching process.

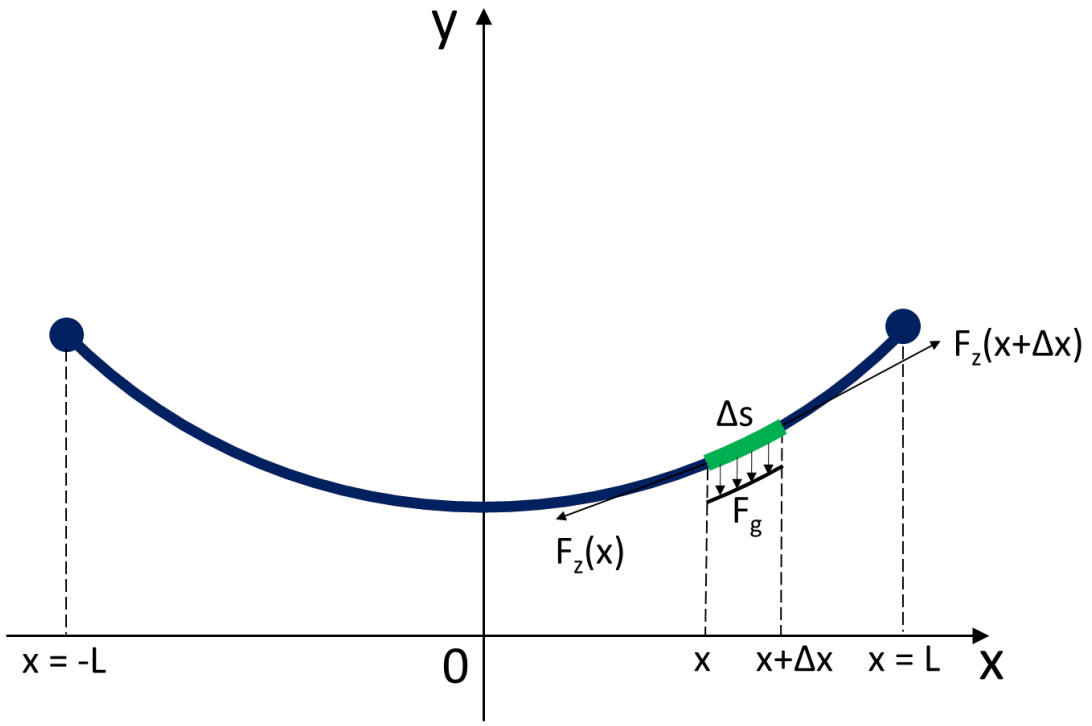

Fig. 3 Visual representation of the bending line of a filament suspended on 2 points and bending due to gravitational force

A hanging filament of constant diameter bends the same way as a chain of constant diameter and weight and can be described by a catenary function. Starting from a simple force balance, equation 11 can be derived for the shape of a catenary (Behroozi, 2014).

$$y(x,t) = \frac{4F_{z,0}(t)}{\rho g \pi D^2(t)} \cosh\left(\frac{\rho g \pi D^2(t)}{4F_{z,0}(t)} x\right) \tag{11}$$

where $y(x,t)$ is the y-coordinate of the filament bending line (average of the top and bottom edge for a specific x-coordinate), x is the horizontal coordinate, ρ is the fluid density, g is the gravitational acceleration, $D(t)$ is the time dependent diameter of the filament, so that $\rho g \pi D^2(t)/4$ represents the time dependent line density of a filament of decaying cross-sectional area $A(t) = \pi D^2(t)/4$. The tension along the filament is denoted F_z and the suffix 0 indicates the position at the minimum. If the minimum of the bending line is moved to the origin of the coordinate system, the equation can be fitted with one parameter a:

$$y(x,t) = a(t) \cdot \left(\cosh\left(\frac{x}{a(t)}\right) - 1\right) \tag{12}$$

where $a(t)$ is the bending parameter

$$a(t) = \frac{F_{z,0}(t)}{\rho g A(t)} \tag{13}$$

A low value for the bending parameter corresponds to a pronounced bending of the filament, whereas a high value indicates a filament to be very straight. The axial force is then simply obtained from the bending parameter via the simultaneously obtained diameter and cross-sectional area of the filament.

The bending line of a catenary can also be approximated by a parabola as done in the work of Sachsenheimer et al. However, in the current work we do not follow this simplification and the assumption of a constant force, but fit the bending line shape rather with the full expression of the catenary of eq. 11. The alternative integration method presented in the Sachsenheimer et al. proved to be very sensitive to the length and position of the fitted filament segment, especially around the minimum and for the very straight filaments of the Boger fluid investigated in this study, and the interpretation of the axial force was therefore not unambiguous.

Limits of the analysis

A first, upper limit for filament diameters that can be fitted (denoted as D_{crit} in the following) is arising from gravitational effects. The interpretation of the axial tension $F_z(t)$ along the filament, its incorporation into the force balance and the resulting pinching laws via the factor

X, is usually done under the assumption that gravitational effects can be neglected. As pointed out by McKinley and Tripathi (McKinley & Tripathi, 2000), gravitational sagging of a vertical filament breaks the symmetry demanded by the similarity solutions, and they defined a Bond number as $\frac{\rho g D^2}{\gamma}$ to determine when a filament diameter D is thin enough (such that the Bond number is below a critical value of 0.1) to neglect gravitational effects. This criterion is expected to hold for relatively short filaments where the axial and radial length scales are still of similar order of magnitude to be represented simply by D. Also for a horizontal filament the similarity solutions only apply once gravitational contributions to the force balance can be neglected. However, for the horizontal filaments considered here the presence of gravitational force is directly observable from the bending (and necessary for the evaluation of the axial tension from the degree of bending as described above), and we evaluate in the following when and if forces along the filament arising from this observed gravitational bending begin to significantly contribute to the axial forces in our force balance (that we consider in eq. 2 to arise only from surface tension and bulk stresses, and no gravitational contribution).

For the horizontal case the axial length scale L cannot be neglected. In a catenary of constant line density along the chain (but time-dependent line density as the filament shrinks), it follows from eq. 11 that the tension along the chain including the gravitational contribution is given by

$$F_z(x,t) = F_{z,0}(t)\cosh\left(\frac{x}{a(t)}\right) \tag{14}$$

The gravitational contribution increases with distance x away from the minimum value $F_{z,0}$ at the middle of the chain (and $F_{z,0}$ contains no gravitational component, since it is acting only perpendicular to the direction of gravitational acceleration). In order to estimate the total extra contribution of the gravity to the axial tension along the whole chain, we integrate eq. 14 over the whole distance from the minimum to the end point $x = L$ of the catenary to obtain an average tension in the filament, $\bar{F}_z(t) = \frac{1}{L}\int_0^L F_z(x,t)dx$, that includes the gravitational contribution. Comparing this now to the axial tension $F_{z,0}(t)$ at the minimum (that carries no gravitational contribution), allows to estimate if the extra gravitational contributions can still safely be neglected for a filament of total axial dimension $2L$:

$$\frac{\bar{F}_z(t)}{F_{z,0}(t)} = \frac{a(t)}{L}\sinh\left(\frac{L}{a(t)}\right) \tag{15}$$

Equalizing $F_{z,0}(t)$ of eq. 13 to the surface tension dependent relation of eq. 6 $F_{z,0}(t) = X\pi\gamma D$ allows to introduce a Bond number

$$Bo = \frac{\rho g D L}{\gamma} = 4X\frac{L}{a(t)} \tag{16}$$

that depends with D and L on both relevant length scales of the filament. The comparison of $\bar{F}_z(t)$ to $F_{z,0}(t)$, expressed as force error percentage

$$\epsilon_F = \frac{\bar{F}_z(t)}{F_{z,0}(t)} - 1 = \left(\frac{4X}{Bo}\sinh\left(\frac{Bo}{4X}\right)\right) - 1 \tag{17}$$

can thus be expressed simply as a function of the this Bond number. Gravitational effects will dominate for large Bond numbers, and thus for the large diameters at the beginning of the experiment. With decreasing diameter and smaller Bond numbers, a Taylor series expansion approximates the error as $\frac{Bo^2}{96X^2}$, which allows to directly calculate a critical Bond number with decaying diameter, below which gravity can be neglected. Setting the boundary for negligible gravitational forces at $\frac{\bar{F}_z(t)}{F_{z,0}(t)} - 1 \approx \frac{Bo^2}{96X^2} \leq \epsilon_{F,min}$ gives a critical value of the Bond number of $Bo_{high} = \sqrt{96X^2\epsilon_{F,min}}$. Assuming the critical value to be reached for Bond numbers of order O(1) results in a relatively small value for the error margin of $\epsilon_{F,min} = 0.001$. From this one can calculate an upper diameter limit, $D_{high} = \frac{Bo_{high}\gamma}{\rho g L} = \sqrt{96\epsilon_{F,min}}\frac{X\gamma}{\rho g L}$. Only for filaments below this limit gravitational contributions to the force balance can be neglected. It should be noted that stretching to longer distances will lower the critical upper diameter limit D_{high} for a given critical Bond number. In the experiments considered in this paper, D_{high} is always larger than the actual filament diameter, even for the large initial diameters after the step stretch, due to the large ratio between final and initial gap in combination with the use of small diameter plates.

It should be noted that all the above considerations to fit the filament as a catenary of constant line density along the chain is strictly valid only for filaments of a constant diameter. While fluids with a dominant elasto-capillary balance quickly acquire a near cylindrical shape, in particular for Newtonian fluids the filament becomes slender only at later stages, so that it is initially not possible to fit the whole filament, but rather only a subsection around the minimum diameter, for which the diameter can be assumed to be constant of the length of this subsection. The catenary description of eq. 12 is principally valid also for any subsection of the filament

that can be considered as slender and meets the constant diameter criterion. To identify a filament subsection with quasi-constant diameter, the following criterion is used

$$D(x) < \max\left(1.05 D_{min}, D_{min} + 1\,px\right) \tag{18}$$

where $D(x)$ is the filament diameter as a function of the horizontal coordinate, D_{min} is the smallest filament diameter observed for this subsection and px is the square pixel dimension of the analyzed image of the filament. The latter criterion remediates the pixel resolution of the camera and objective for very small diameters, which is for the current set-up 2.49 µm/px. This pixel dimension is chosen to be large enough, so that all or nearly all 2048 horizontal pixels are used for the observation of the stretched distance of 6.5 mm, but still sufficiently small to resolve the bending of even the very straight filaments of the Boger fluid investigated in this study. To account for the still slightly varying diameter with the boundaries of eq. 18, the axial force in eq. 13 is calculated using the average cross-sectional area of the considered filament part.

The second criterion in eq. 18 is also pointing at a second, lower limit for the filament diameter (denoted as D_{low} in the following): the increasing straightening of the filament with with thinning will eventually prohibit a fitting of the catenary as one approaches the resolution limits to measure the vertical deflection or bending of the horizontal filament. The determination of the diameter at which this limit is reached is in particular important for the investigation of the very straight filaments observed for the elasto-capillary balance regime of the Boger fluid investigated in this study. But also having to choose a lower length of the filament subsection in order to meet the slenderness criterion of eq. 18 will in turn lead to a lower vertical deflection over the length of that filament segment due to gravitational bending, and therefore also lowers the accuracy of the fit of eq. 12 to the shorter bending line, similar to the increasing straightening with time. A criterion for the possibility to still accurately fit the bending line would be the maximum change of the vertical bending line position $\Delta y = y(x = L) - y(x = 0)$ over the fitted length L. From eq. 12 with $F_{z,0}(t) = X\pi\gamma D$ and the definition of the Bond number of eq. 16 one obtains

$$\frac{\Delta y}{L} = \frac{4X}{Bo}\left(\cosh\left(\frac{Bo}{4X}\right) - 1\right) \tag{19}$$

For small Bond numbers, a series expansion approximates this as $\frac{\Delta y}{L} \approx \frac{Bo}{8X}$, so that generally with decreasing filament diameter Δy gets smaller, and the resolution of the determined axial

force decreases towards the end of a pinching experiment. Furthermore, the series expansion of eq. 19 indicates that Δy depends quadratically on the selected filament segment length L. Furthermore, the inverse dependency on the factor X indicates that elasto-capillary balance controlled filaments with a larger X will lead to straighter filaments and smaller Δy than for filaments of Newtonian liquids. However, it should be noted that at the same time the elastic filaments are generally more slender, which leads to longer filament segments L that meet the diameter criterion of eq. 18, which partially compensates for the loss of resolution through the straightening.

From a practical point of view, experimentally determined bending line deflections could be reliably fitted down to $\frac{\Delta y}{L} \approx \frac{L}{2a} \geq \frac{1}{1000} = 0.001$. With eqs. 16 and 19 and the simplification for small Bond numbers, this gives a practical lower fitting limit of also $\frac{Bo}{8X} \geq 0.001$, or a lower fitting limit for the diameter $D_{low,fit} \geq 0.008 \frac{X\gamma}{\rho g L}$.

A general lower resolution limit for detecting Δy is then set by the pixel dimension px. In order to properly perform a fit, a filament deflection of at least one pixel is required, or $\Delta y \approx \frac{L^2}{2a} \geq 1\ px$, which yields again with eqs. 16 and 19 for small Bo a lower limit of $\frac{Bo\ L}{8X\ px} \geq 1$, and thus a lower diameter limit of $D_{low,res} \geq \frac{8X\gamma}{\rho g L^2} px$. This equation yields a general lower limit for $D_{low,res}$ of order O(5 μm) when fitting over the maximum experimental range of L = 3.25 mm, using the smaller pixel dimension px = 2.49 μm and the relevant theoretical parameter X for a Newtonian or elastocapillary pinching (or a lower Bond number limit of Bo = O(0.01)). It should be noted that it is this smaller pixel dimension and increased resolution of the filament bending line in comparison to previous studies on forces in horizontally bending filaments that enables the investigation of the relatively straight filaments observed for example for the Boger fluids in this study. Furthermore, it should be noted that this lower diameter limit rises when fitted over the shorter lengths L arising from the slenderness criterion of eq. 18.

Important to note is that the proposed diameter limits $D_{high}, D_{low,fit}$ and $D_{low,res}$ depend on the axial force (via the X-factor) and considered filament length satisfying eq. 18. These diameter limits are thus not perfect constants and vary throughout the experiment depending on the measured axial force and filament slenderness. Consequentially, the validation of the

diameter criteria needs to be conducted for every frame separately as the criteria will evolve over time.

Examples of the fitting of the bending line for PDMS5 and the PIB Boger fluid are given in figure 4, together with images of the respective filament with an overlay of the detected edges of the filaments (in red) over the axial distance for which the slenderness criterion of eq. 18. Both graphs show qualitatively with a magnified view of the vertical distance of the stepped bending line that the high vertical pixel resolution of 2.49 µm/px is indeed required in order to sufficiently resolve the bending over the axial distance for which the filament can be considered slender (and show that indeed $\Delta y \approx \frac{L^2}{2a} \geq 1\ px$, as required for the definition $D_{low,res}$). The eligibility of the fit can then be quantified from the obtained eqs. 17 and 18 and the ratio of fitted length L to the fitting bending parameter a (or the Bond number $Bo/8X = L/2a$) of 0.0596 and 0.0114, which are clearly beneath the critical limit of 0.001 (and the diameters of 241 µm and 37 µm are clearly above the limits D_{low} of 36 µm and 27 µm). The fits clearly approximate the bending lines well with R2-fitting values of 0.7 and 0.93, respectively.

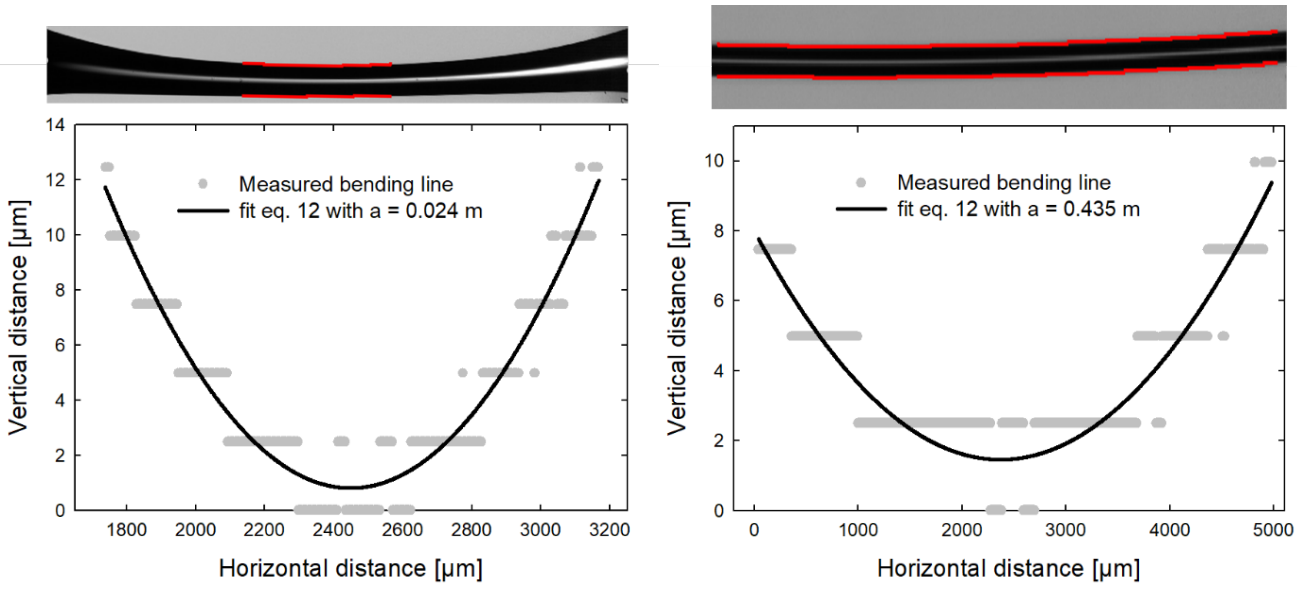

Fig. 4 Fitting of the bending line of a hanging fluid filament. Left: PDMS5. Right: PIB Boger fluid. The red outlines on the filament images represents the horizontal range over which the slenderness criterion of eq. 18 is fulfilled and over which the bending line in the graphs is given, and subsequently fitted with eq. 12 to yield the bending parameter a

Finally, a comparison of the lower limit criteria, as for example the ratio of limiting diameters $\frac{D_{low,fit}}{D_{low,res}} = \frac{L}{1000\,px}$, shows that one can simply use the ratio of fitted length L to the pixel dimension px in order to determine which lower diameter limit will be applicable. With the front factor 1/1000 and the pixel resolution used in the current work of px = 2.49 µm, one expects the fitting limit to dominate only for filaments with fitted lengths L longer than 2490 µm. In figure 4a the Newtonian sample PDMS5 could be fitted over a total distance of 1430 µm (where the maximum fitted length L = 715 µm is determined by the slenderness criterion of eq. 18). With L shorter than the critical value of 2490 µm, the lower limit is thus expected to be the resolution limit. However, both the Bond number for the fitting limit $\frac{Bo}{8X}$ = 0.0145 and for the resolution limit $\frac{BoL}{8X\,px}$ = 4.07 (calculated from the fluid and geometrical parameters of the fitted filament) are clearly larger than their critical values of 0.001 and 1, respectively. And also the observed bending over the fitted length of $\frac{\Delta y}{L} \approx \frac{L}{2a} = 0.0136$ and the deflection over the pixel size of $\frac{\Delta y}{px} = 5$ agree well with these numbers.

Only for very straight filaments will the fit be limiting. Figure 4b shows with the PIB Boger fluid and its very slender shape such an extreme case. Here, eq. 18 allows a fit over a much longer distance of L = 2430 µm, which is very close to the limit of 2490 µm and therefore the resolution limit is very close to the limit of the fit. This becomes clear from the absolute data, since the observed $\frac{\Delta y}{L} \approx \frac{L}{2a} = 0.0028$ is close to the limiting value of 0.001, while the detected deflection in figure 4b is with $\frac{\Delta y}{px}$ = 3 even for the high optical resolution of the current setup just above the critical value of 1. Finally it should be noted that also in this case the Bond number calculations of $\frac{Bo}{8X}$ = 0.0030 and $\frac{BoL}{8X\,px}$ = 2.93 predict the observed bending well.

Results and discussion

PDMS 5 Pa·s

For Newtonian liquids, McKinley and Tripathi indicated the validity of the X-factor of 0.7127 predicted by Papageorgiou, which was experimentally verified by Sachsenheimer et al. (McKinley & Tripathi, 2000; Sachsenheimer et al., 2012). In order to validate the current set-up and evaluation procedure of the axial force, experiments were conducted with a Newtonian

PDMS oil with a measured viscosity of 5.8 Pa·s, for which a pinching time on the order of seconds assures stable and observable filaments, in order to extract the X-factor accurately and to compare to the known Newtonian value. The results of 3 experiments are summarized in figure 5 as to indicate reproducibility of the measurements. The time of break-up is set equal to t = 0 to collapse the curves onto a single one during the relevant pinching stages. Figure 5a shows the decrease of the minimal diameter over time, which appears quasi-linear as expected for Newtonian fluids in the V-regime from eq. 7 (the inertia-viscous (IV) regime of eq. 7 with $X = 0.5912$ will not be observed at later times as predicted from the geometrical parameters of the filament as introduced by Verbeke et al. (Verbeke et al., 2020)). However, a closer comparison to the theoretical thinning of the VC-regime of eq. 7 using the actual viscosity and the X-factor of 0.7127 of Papageorgiou (straight line in figure 5a) shows that this linear decay is just attained at a later stage (after -250 ms).

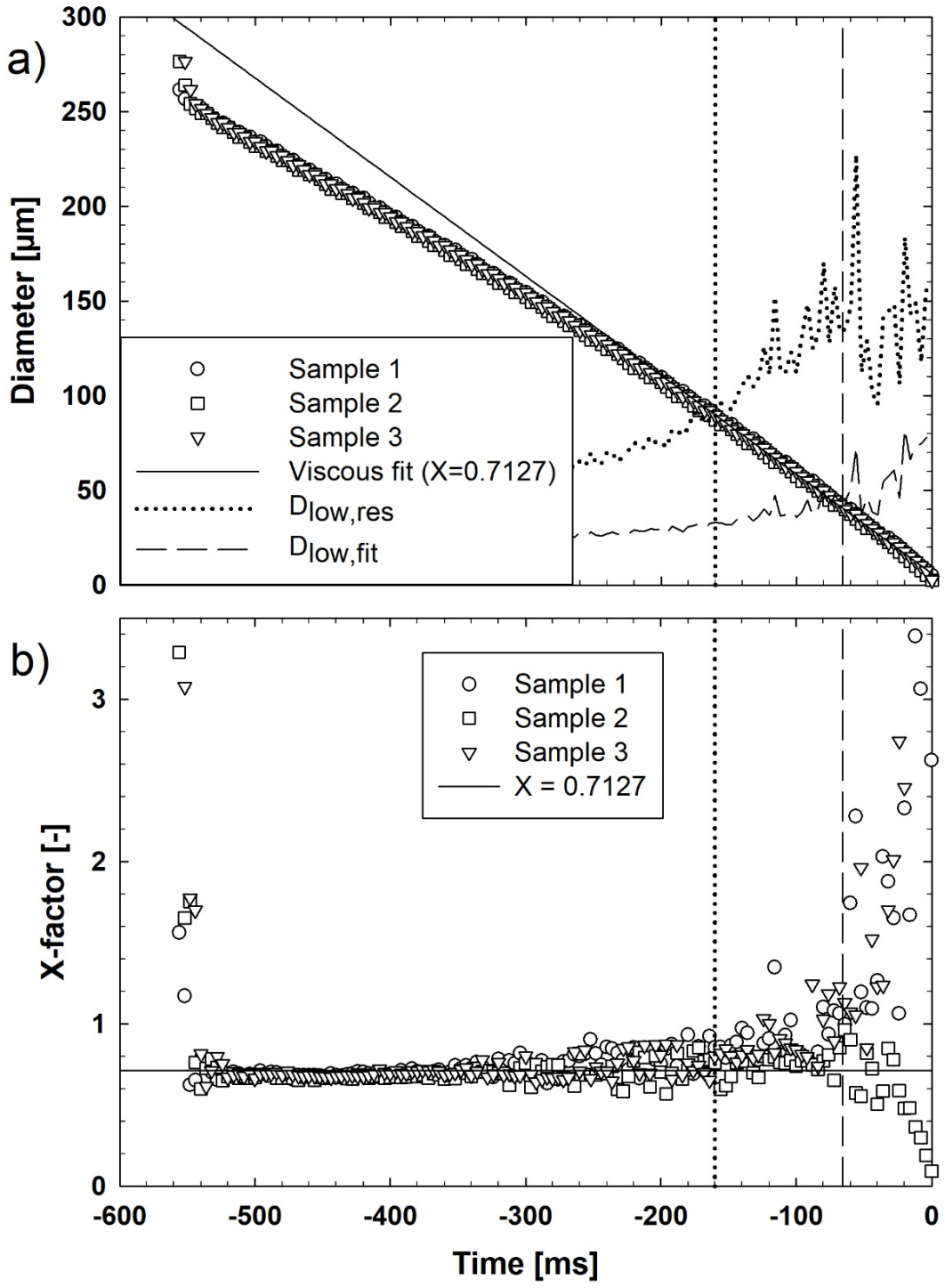

Fig. 5 Minimal diameter and X-factor evolution over time. The diameter limits determined for the dimensions of each individually fitted filament image are given in the top graph as an average of the 3 samples. The actual critical diameters from the intersection with the limiting values are given as vertical lines in both graphs. The X-factor of 0.7127 is indicated with a solid line

The independently determined axial force data from the filament bending and the resulting X-factor are directly supporting this observation. As can be seen in figure 5b, the measured X-factor is initially constant, however the high resolution allows to observe that it is with 0.67 lower than the Papageorgiou solution. A lower initial predicted X-factor was predicted by McKinley and Tripathi, based on the earlier work of Kolte and Szabo. They show numerically that X is approaching the Papageorgiou solution only asymptotically at later stages. Our lower initial value of 0.67 agrees well and confirms now experimentally their predicted lower X-value during the initial pinching regime. These observations demonstrate again that for the quantitative measurement of an extensional viscosity the use of the correct (experimentally determined) X-factor is crucial, and that the use of a general similarity solution as the Papageorgiou one for Newtonian fluids should only be applied at later pinching stages when the similarity solution is finally approached. The expected X-factor can be calculated based on the pinching curve following eq. 9 in the paper of McKinley and Tripathi. The measured values correspond very well to the theoretical ones indicating a proper working of the analysis.

At later stages, the X-factor rises as expected. The postulated X-factor of 0.7127 by Papageorgiou is not clearly visible due to scatter on the data. Further fine tuning of the device is required to analyze these data points properly.

Figure 5a also contains the limiting values for the diameters D_{high}, $D_{low,fit}$ and $D_{low,res}$, that indicate the range in between which the diameter is small enough that gravity can be neglected, but still sufficiently large to have a reliably detectable bending. The importance of the limits becomes obvious in particular when approaching break-up (and diameters are smaller than $D_{low,res}$), where results for X start to scatter significantly due to an increasingly straight filament that causes the deflection $\frac{\Delta y}{L}$ to approach the resolution limit of the set-up and prevents an interpretation of force and X data outside the limits.

PIB Boger Fluid

With the applicability of the force determination and its limits tested for the Newtonian model case, we are now able to probe the so far only theoretically predicted axial force evolution of a very dilute polymer solution, for which in eq. 6 an X-factor of 1.5 was arising from a similarity solution of Clasen et al. (Bhat et al., 2012; Clasen, Eggers, et al., 2006). For the chosen Boger

fluid with a high solvent viscosity, residual effects of inertia can be neglected, and its high relaxation time leads to very stable fluid bridges lasting for several seconds and even minutes, enabling an accurate observation of the pinching and bending dynamics, limited only by the above derived resolution and deflection limits.

Figure 6a shows the evolution of the minimal diameter over time on a semilog scale. During an initial period after the stretch of ~20 s for each sample the filament is still acquiring its slender conformation. After that the diameter evolution follows the exponential pinching profile of eq. 8 for an intermediate period up to ~100 s before breakup, indicating in this regime the applicability of Oldroyd-B type constitutive model for which the similarity solution was derived. For the last ~100 s the filament diameter starts to decay faster than the exponential pinching which is attributed to the onset of finite extensibility effects of the unraveling polymer, which has been successfully modelled expanding the Oldroyd-B to a finitely extensible nonlinear elastic dumbbell (or FENE) model (Clasen, Plog, et al., 2006; Entov & Hinch, 1997). Figure 6b shows the independently measured X-factor obtained from each pinching profile as a function of time, and it is clear that the experimental data qualitatively confirm the theoretical X-value of 1.5 in the exponential pinching regime. However, it is also clear that this value is not approached right away, but only later in the exponential thinning regime. Although the slender filament shape and thus applicability of the similarity solution (indicated by the exponential decay) is attained relatively early (~50 s after the initial step stretch for each experiment in figure 6b), Bhat et al. have pointed out that the complete similarity solutions should also account for the capillary pressure in the end droplets. While this becomes eventually subdominant to the pressure developing in the pinching filament, this can possibly affect the axial tension at earlier stages. The total bulk stress contribution to eq. 2 of the thinning Oldroyd-B filament is then $\sigma_{zz} - \sigma_{rr} = \frac{4\gamma}{D} - \frac{4\gamma}{R_{drop}}$, where the second term on the right hand side accounts for the capillary back-pressure of the end droplets of radius R_{drop} into the bulk filament (Bhat et al., 2012). This effectively lowers the bulk stress, and leads thus to a lower value for $X = 1.5 - \frac{D}{R_{Drop}}$. However, the end droplet radius R_{drop} remains nearly constant over the course of the experiment, since the amount of fluid entering from the filament is small compared to the end droplet volume, in particular after the similarity solution is attained. The factor X approaches this with decreasing filament diameter D eventually the limiting value of 1.5. For the specific case and geometrical parameters of the experiments in

Figure 6, the end droplet radius can be approximated by the radius of the endplates of 1 mm, leading to an initial value of X for the initial filament diameters of ~200 um (once the slender shape has been acquired) shown in figure 6 of $X = 1.5 - \frac{0.2\ \mathrm{mm}}{1\ \mathrm{mm}} = 1.3$, which develops until the visible onset of finite extensibility effects at filament diameters of ~50 um to $X = 1.5 - \frac{0.05\ \mathrm{mm}}{1\ \mathrm{mm}} = 1.45$

The deviation from the exponential decay in figure 6a and the faster decay is usually attributed to the approach of the finite extensibility limit of the unraveling polymer chains. (Anna et al., 2001; Mathues et al., 2018; Szabo, McKinley, & Clasen, 2012) Numerical calculations (Clasen, Plog, et al., 2006) for the Oldroyd-B model, expanded to a FENE model, predict a faster than exponential growth of the bulk stresses in the thinning filament in the approach of the finite extensibility limit. However, the calculations also predict a similar increase in capillary pressure, so that X should not be affected by finite extensibility within the resolution limit indicated in figure 6b.

Figure 6b also contains the upper and lower limits, and it is again clear that the strong scatter and apparent deviation of X to higher values close to the breakup of the filament is indeed within the regime below the resolution limit where interpretation is ambiguous.

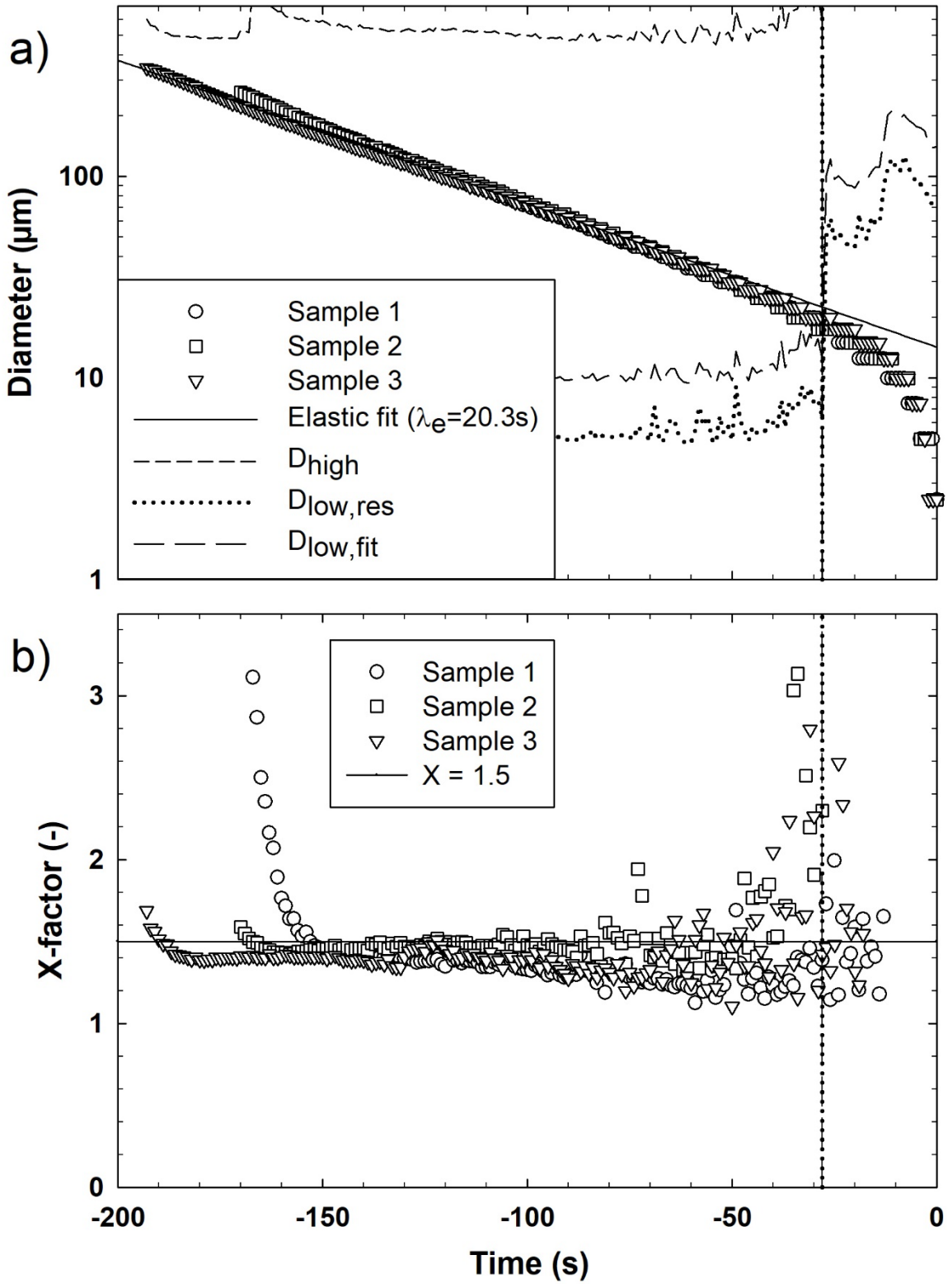

Fig. 6 Minimal diameter and X-factor evolution over time for the Boger fluid. The diameter limits determined for the dimensions of each individually fitted filament image are given in the top graph as an average of the 3 samples. The actually critical diameters from the intersection with the limiting values are given as vertical lines in both graphs. The X-factor of 1.5 is indicated with a solid line

Similarly, the initial upturns at the beginning of the experiments are beyond the indicated upper limit and attributed to the fact that the filament is still being stretched or hasn't found its stable position yet. Similar to the case of the Newtonian fluid, also this case demonstrates the utility of independently measuring the evolution of the tension and X-factor in order to determine the regime in which the similarity solutions strictly hold in order to extract material functions, as in this case the relaxation time via eq. 8 as indicated in figure 6a.

Dilute PS solution

The diameter evolution of the dilute polymer solution of 0.1 wt% PS6M in DEP is shown in figure 7a. The time to break-up is shorter for these solutions (≈50 ms) due to the lower solvent viscosity. Due to the lower viscosity, a strike time of 100 ms is employed instead of the standard 40 ms, to reduce inertia induced oscillations in the filament. With these adaptations of the measurement protocol, reproducible pinching data are obtained, and also here an exponential pinching regime can be identified at earlier times similar to the dilute PIB Boger fluid. However, this dilute polymer solution does not attain the X-factor of 1.5 as the PIB Boger fluid, but a lower value of $X = 1.1$ is determined within the limits of reliable fitting of the bending filament. Although the exponential thinning is still indicating the excitation of a single relaxation process (Entov & Hinch, 1997), the solution with a concentration of 0.588 c^* is not following the similarity solution of a dilute case with $X = 1.5$ and described by a simple FENE model anymore, as has already been hinted as for example in the work of Clasen et al. (Clasen, Eggers, et al., 2006)

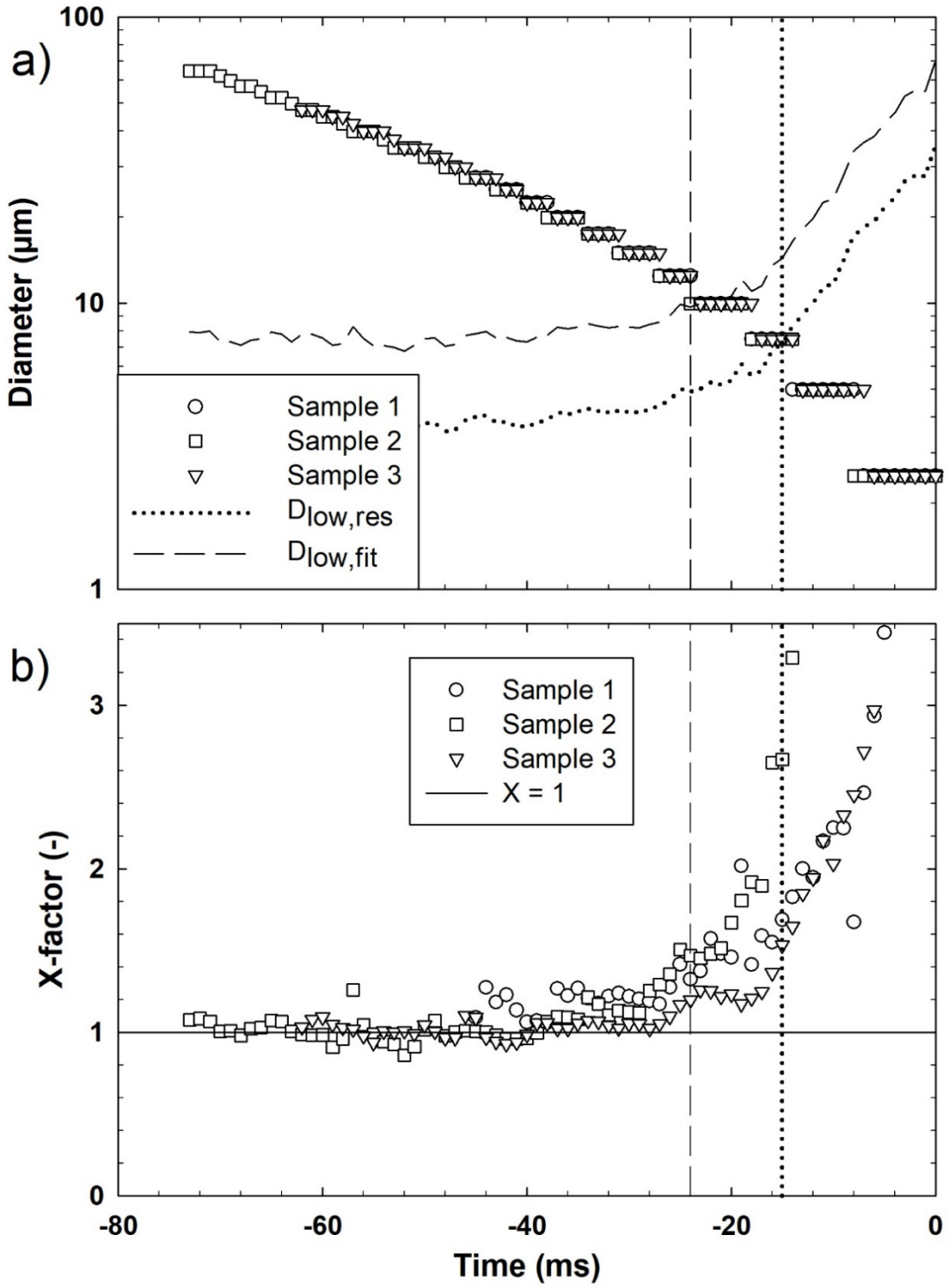

Fig. 7 Minimal diameter and X-factor evolution over time for the dilute PS solution. The diameter limits determined for the dimensions of each individually fitted filament image are given in the top graph as an average of the 3 samples. The actual critical diameters from the intersection with the limiting values are given as vertical lines in both graphs. The X-factor of 1 is indicated with a solid line

Semi-dilute PS solution

For the semi-dilute PS solution, the deviation of the X-factor from the limiting case of 1.5 for dilute systems becomes even more apparent. The diameter and force factor data for this case are shown in figure 8. Also here the diameter evolution exhibits clearly an exponential decay similar to an EC-regime. However, in this case, the independently determined X-factor values start at around 1.2 and seem to slowly decrease to a value of around 1 before break-up.

Since the behavior of semi-dilute polymer solutions under extensional flow is practically uninvestigated, only hypotheses can be made on the physical nature of the internal dynamics which might explain this behavior. A potential hypothesis is that the entanglements unravel under the influence of the extensional flow and reduce the force in the filament and thus the X-factor. Also Sachsenheimer et al. recorded X-factor value of around 1 for several semi-dilute unentangled polymer solutions of PEO in water (Sachsenheimer et al., 2012, 2014). Potentially the fluid moves to a new found steady-state similar to those observed in their work.

The large ‘bump’ at the end for 2 of the 3 measurements is due to inertial after-effects originating from a shorter strike time and the resulting oscillations of the end droplets caused by the sudden de-acceleration of the endplates at the end of the strike. The three samples had different respective strike time of 40, 20 and 100 ms. The images of the former 2 experiments show a larger up- and downward movement of the filament over the course of the experiment than the latter experiment with the longest strike time, pointing at the importance of a well-tuned motion profile with a minimal deceleration of the moving plate. It is interesting to note that the effect of the moving filament is dominantly present in the beginning and end of the experiment but has a less dominant effect during the middle of the pinching.

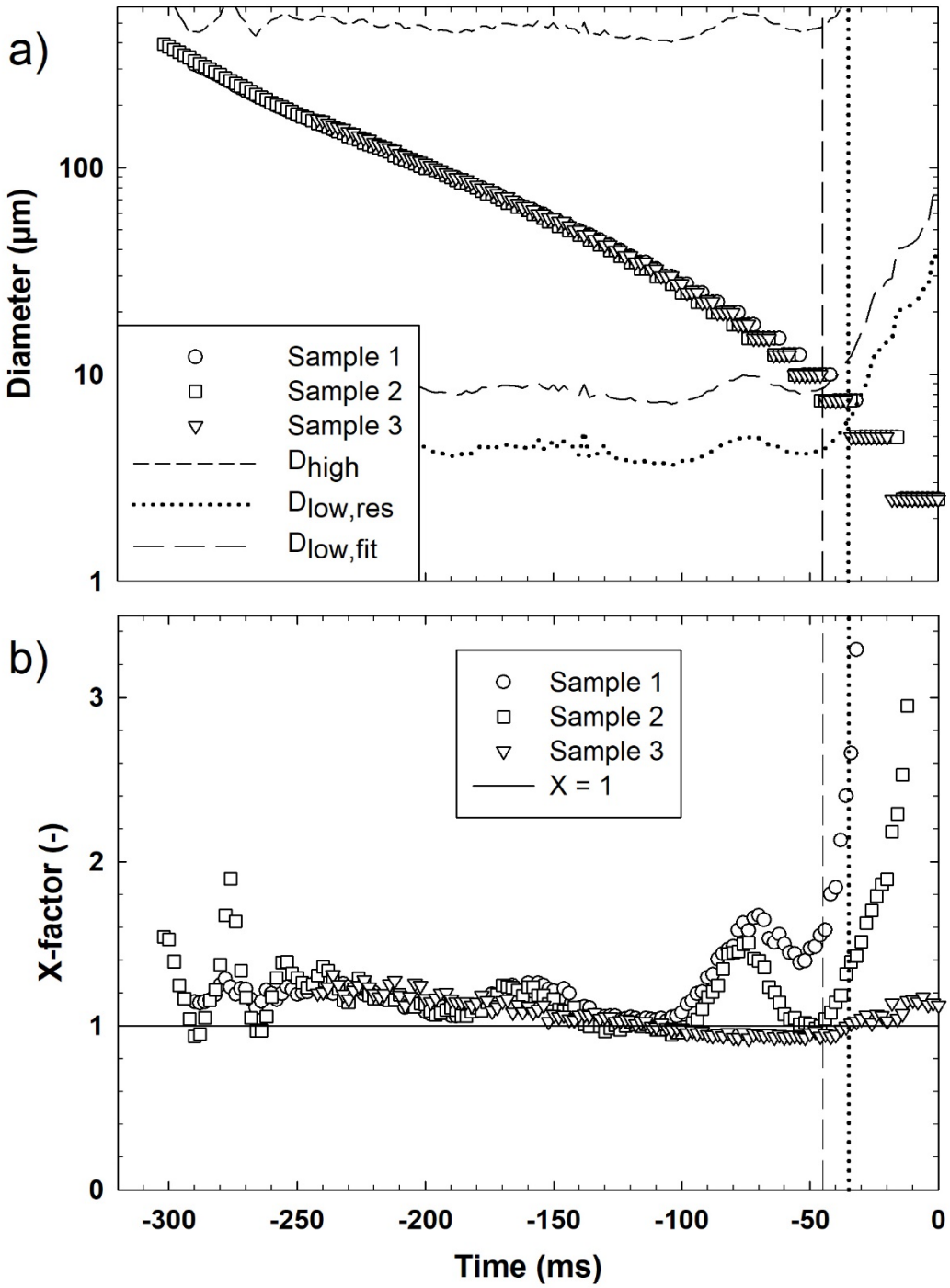

Fig. 8 Minimal diameter and X-factor evolution over time for the semi-dilute PS-solution. The diameter limits determined for the dimensions of each individually fitted filament image are given in the top graph as an average of the 3 samples. The actual critical diameters from the intersection with the limiting values are given as vertical lines in both graphs. The X-factor of 1 is indicated with a solid line

Semi-dilute PEO solution

The second semi-dilute polymer solution tested in addition to the semi-dilute PS solution is also low viscous but consists of different polymers. The molecular weights of the long polymer chains are comparable for both solutions. The added high molecular weight chains' absolute concentration greatly differs from that of the semi-dilute PS, but differs only slightly when comparing to the overlap concentration (see table 1). .

Figure 9 shows the results of this semi-dilute PEO solution in terms of diameter and X-factor evolution. A first observation to make is that the X-factor data follow a similar trend as for the semi-dilute PS polymer solution. An initial start slightly above 1 after which the force in the filament slowly decreases over the duration of the experiment. By the end of the reliability window, the X-factor has dropped to a value of around 0.9. Once $D_{low,res}$ has passed, the data starts to scatter more and the data can no longer be relied on.

These results show the limited impact on the axial force of using a different polymer-solvent combination. Due to the similarity in axial force, it is likely that these two semi-dilute solutions exhibit the same unraveling mechanisms.

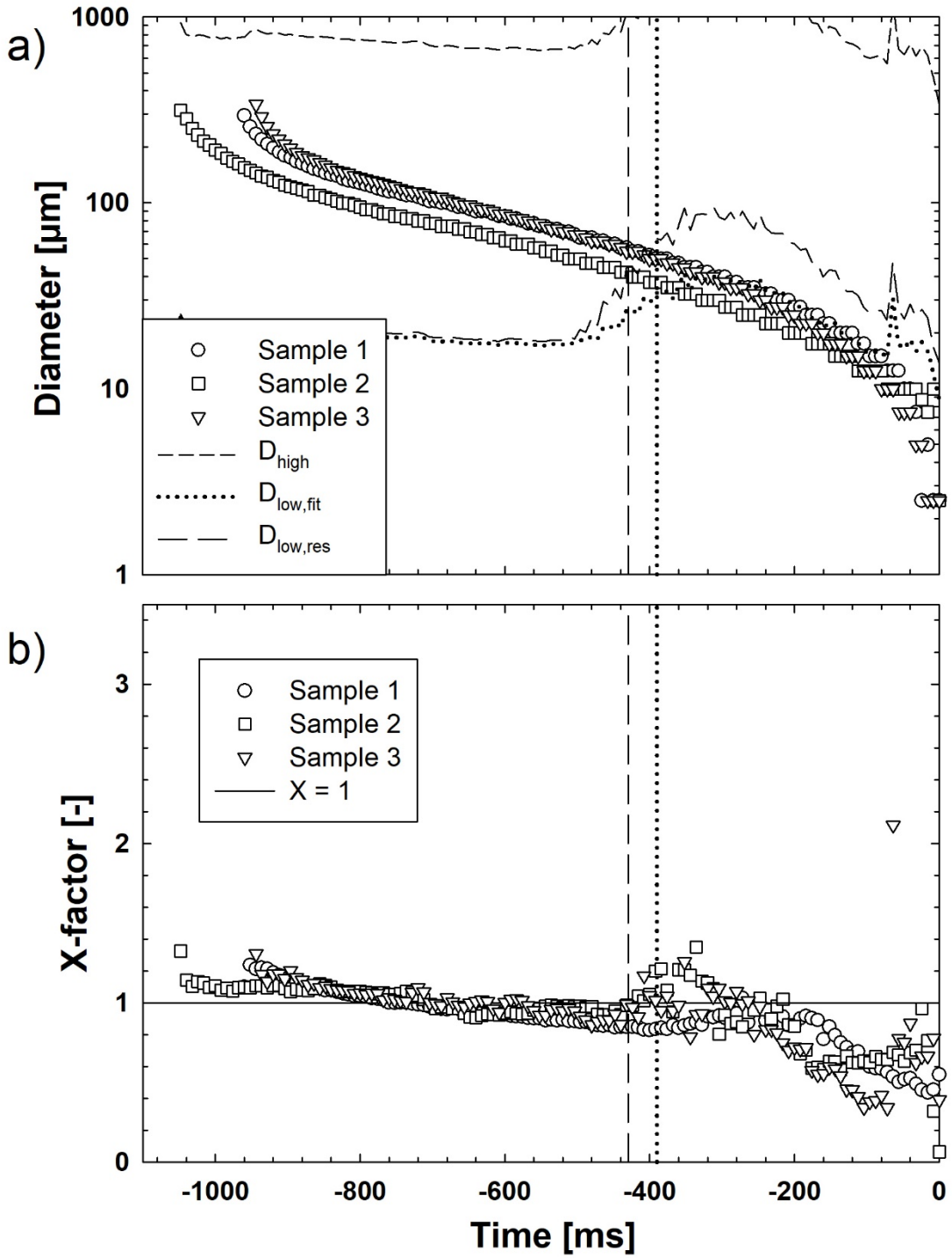

Fig. 9 Minimal diameter and X-factor evolution over time for the semi-dilute PEO solution. The diameter limits determined for the dimensions of each individually fitted filament image are given in the top graph as an average of the 3 samples. The actual critical diameters from the intersection with the limiting values are given as vertical lines in both graphs. An X-factor of 1 is indicated with a solid line

Conclusion

In this paper a new device for executing capillary pinching experiments of horizontal fluid filaments is presented, together with a precise method of extracting axial forces in the fluid filament from fitting the bending of the filament with the full expression of a catenary. The device and method are validated using a purely viscous liquid of known extensional viscosity and axial forces. This also allowed to confirm the theoretical upper and lower limits of the filament diameter to reliably extract the axial force as a result of the material properties under extensional flow. This validation allowed then to probe a viscoelastic solution in form of a truly dilute polymer solution (a Boger fluid), which allowed to experimentally approach for the first time the theoretical prediction of Clasen et al. (Clasen, Eggers, et al., 2006) of the axial force evolution and the force factor $X = 1.5$ for dilute polymer solutions. Finally, the applicability of the new test method and its limits were experimentally explored for less accessible, low viscosity dilute and semi-dilute solutions. Although still following an exponential decay of the pinching filament, typical for dilute solutions, these fluids exhibited a lower X-factor of around 1 to 1.2, while the cause of this deviation still remains to be explored.

Acknowledgment

The authors would like to acknowledge financial support from the ‘Bijzonder Onderzoeksfonds KU Leuven’ (GOA 15/007).

Conflicts of interest/Competing interests

No conflicts of interest or competing interests are present for the publication of this paper.

References

Anna, S. L., McKinley, G. H., Nguyen, D. A., Sridhar, T., Muller, S. J., Huang, J., & James, D. F. (2001). An interlaboratory comparison of measurements from filament-stretching rheometers using common test fluids. *Journal of Rheology*, *45*(1), 83–114. https://doi.org/10.1122/1.1332388

Arnolds, O., Buggisch, H., Sachsenheimer, D., & Willenbacher, N. (2010). Capillary breakup extensional rheometry (CaBER) on semi-dilute and concentrated polyethyleneoxide (PEO) solutions. *Rheologica Acta*, *49*(11), 1207–1217. https://doi.org/10.1007/s00397-010-0500-7

Bazilevsky, A. V., Entov, V. M., & Rozhkov, A. N. (1990). Liquid filament microrheometer and some of its applications. *Third European Rheology Conference*, 41–43.

Behroozi, F. (2014). A fresh look at the catenary. *European Journal of Physics*, *35*(5). https://doi.org/10.1088/0143-0807/35/5/055007

Bhardwaj, A., Miller, E., & Rothstein, J. P. (2007). Filament stretching and capillary breakup extensional rheometry measurements of viscoelastic wormlike micelle solutions. *Journal of Rheology*, *51*(4), 693–719. https://doi.org/10.1122/1.2718974

Bhat, P. P., Appathurai, S., Harris, M. T., & Basaran, O. A. (2012). On self-similarity in the drop-filament corner region formed during pinch-off of viscoelastic fluid threads. *Physics of Fluids*, *24*(8). https://doi.org/10.1063/1.4745179

Boger, D. V. (1977). A highly elastic constant-viscosity fluid. *Journal of Non-Newtonian Fluid Mechanics*, *3*(1), 87–91. https://doi.org/10.1016/0377-0257(77)80014-1

Bousfield, D. W., Keunings, R., Marrucci, G., & Denn, M. M. (1986). Nonlinear analysis of the surface tension driven breakup of viscoelastic filaments. *Journal of Non-Newtonian Fluid Mechanics*, *21*(1), 79–97. https://doi.org/10.1016/0377-0257(86)80064-7

Brenner, M. P., Lister, J. R., & Stone, H. A. (1996). Pinching threads, singularities and the number 0.0304. *Physics of Fluids*, *8*(11), 2827–2836. https://doi.org/10.1063/1.869086

Cardinaels, R. (2010). Droplet deformation, breakup and coalescence in shear flow: Effects of confinement and component viscoelasticity.

Clasen, C. (2010). Capillary breakup extensional rheometry of semi-dilute polymer solutions. *Korea-Australia Rheology Journal*, *22*(4), 331–338.

Clasen, C., Eggers, J., Fontelos, M. A., Li, J., & McKinley, G. H. (2006). The beads-on-string structure of viscoelastic threads. *Journal of Fluid Mechanics*, *556*, 283–308. https://doi.org/10.1017/S0022112006009633

Clasen, C., Phillips, P. M., Palangetic, L., & Vermant, J. (2011). Dispensing of Rheologically Complex Fluids: The Map of Misery. *AICHE Journal*, *61*(3), 857–866. https://doi.org/10.1002/aic

Clasen, C., Plog, J. P., Kulicke, W.-M., Owens, M., Macosko, C., Scriven, L. E., … McKinley, G. H. (2006). How dilute are dilute solutions in extensional flows? *Journal of Rheology*, *50*(6), 849–881. https://doi.org/10.1122/1.2357595

Cooper-White, J. J., Fagan, J. E., Tirtaatmadja, V., Lester, D. R., & Boger, D. V. (2002). Drop formation dynamics of constant low-viscosity, elastic fluids. *Journal of Non-Newtonian Fluid Mechanics*, *106*(1), 29–59. https://doi.org/10.1016/S0377-0257(02)00084-8

Dinic, J., Biagioli, M., & Sharma, V. (2017). Pinch-off dynamics and extensional relaxation times of intrinsically semi-dilute polymer solutions characterized by dripping-onto-substrate rheometry. *Journal of Polymer Science, Part B: Polymer Physics*, *55*(22), 1692–1704. https://doi.org/10.1002/polb.24388

Dinic, J., Jimenez, L. N., & Sharma, V. (2017). Pinch-off dynamics and dripping-onto-substrate (DoS) rheometry of complex fluids. *Lab on a Chip*, *17*(3), 460–473. https://doi.org/10.1039/c6lc01155a

Dirking, T., Willenbacher, N., & Boggs, L. (2001). Elongational flow behavior of automotive coatings and its relation to atomization and mottling. *Progress in Organic Coatings*, *42*(1–2), 59–64. https://doi.org/10.1016/S0300-

9440(01)00151-5

Dontula, P., Pasquali, M., Scriven, L. E., & Macosko, C. W. (1997). Can extensional viscosity be measured with opposed-nozzle devices? *Rheologica Acta*, *36*(4), 429–448. https://doi.org/10.1007/BF00396329

Dunlap, P. N., & Leal, L. G. (1987). Dilute polystyrene solutions in extensional flows: Birefringence and flow modification. *Journal of Non-Newtonian Fluid Mechanics*, *23*(C), 5–48. https://doi.org/10.1016/0377-0257(87)80009-5

Eggers, J. (1993). Universal pinching of 3D axisymmetric free-surface flow. *Physical Review Letters*, *71*(21), 3458–3460. https://doi.org/10.1103/PhysRevLett.71.3458

Eggers, J. (1997). Nonlinear dynamics and breakup of free-surface flows. *Review of Modern Physics*, *69*, 865–929. Retrieved from papers2://publication/uuid/1329B18C-197E-4787-8771-930B99E1706E

Eggers, J., & Dupont, T. F. (1994). Drop Formation in a One-Dimensional Approximation of the Navier-Stokes Equation. *Journal of Fluid Mechanics*, *262*(1994), 205–221. https://doi.org/10.1017/S0022112094000480

Entov, V. M., & Hinch, E. J. (1997). Effect of a spectrum of relaxation times on the capillary thinning of a filament of elastic liquid. *Journal of Non-Newtonian Fluid Mechanics*, *72*(1), 31–53. https://doi.org/10.1016/S0377-0257(97)00022-0

Entov, V. M., & Yarin, A. L. (1984). Influence of elastic stresses on the capillary breakup of jets of dilute polymer solutions. *Fluid Dynamics*, *19*(1), 21–29. https://doi.org/10.1007/BF01090901

Fong, H., Chun, I., & Reneker, D. H. (1999). Beaded nanofibers formed during electrospinning. *Polymer*, *40*(16), 4585–4592. https://doi.org/10.1016/S0032-3861(99)00068-3

Fontelos, M. A., & Li, J. (2004). On the evolution and rupture of filaments in Giesekus and FENE models. *Journal of Non-Newtonian Fluid Mechanics*, *118*(1), 1–16. https://doi.org/10.1016/j.jnnfm.2004.02.002

Fuller, G. G., Cathey, C. A., Hubbard, B., & Zebrowski, B. E. (1987). Extensional Viscosity Measurements for Low-Viscosity Fluids. *Journal of Rheology*, *31*(3), 235–249. https://doi.org/10.1122/1.549923

García, F. J., & Castellanos, A. (1994). One-dimensional models for slender axisymmetric viscous liquid jets. *Physics of Fluids*, *6*(8), 2676–2689. https://doi.org/10.1063/1.868157

Graessley, W. W. (1980). Polymer chain dimensions and the dependence of viscoelastic properties on concentration, molecular weight and solvent power. *Polymer*, *21*(3), 258–262. https://doi.org/10.1016/0032-3861(80)90266-9

Hendricks, J. (2019). *Supramolecular Polymeric Solutions in Shear and Extensional Flows*. KU Leuven.

Hoath, S. D. (2016). *Fundamentals of Inkjet Printing: The Science of Inkjet and Droplets*. Wiley-VCH.

Klein, C. O., Naue, I. F. C., Nijman, J., & Wilhelm, M. (2009). Addition of the force measurement capability to a commercially available extensional rheometer (Caber). *Soft Materials*, *7*(4), 242–257. https://doi.org/10.1080/15394450903344603

Lagnado, R. R., & Leal, L. G. (1990). Visualization of three-dimensional flow in a four-roll mill. *Experiments in Fluids*, *9*(1–2), 25–32. https://doi.org/10.1007/BF00575332

Lang, C., Hendricks, J., Zhang, Z., Reddy, N. K., Rothstein, J. P., Lettinga, M. P., … Clasen, C. (2019). Effects of particle stiffness on the extensional rheology of model rod-like nanoparticle suspensions. *Soft Matter*, *15*(5), 833–841. https://doi.org/10.1039/c8sm01925h

Li, J., & Fontelos, M. A. (2003). Drop dynamics on the beads-on-string structure for viscoelastic jets: A numerical study. *Physics of Fluids*, *15*(4), 922–937. https://doi.org/10.1063/1.1556291

Mathues, W., Formenti, S., McIlroy, C., Harlen, O. G., & Clasen, C. (2018). CaBER vs ROJER—Different time scales for the thinning of a weakly elastic jet. *Journal of Rheology*, *62*(5), 1135–1153. https://doi.org/10.1122/1.5021834

McKinley, G. H. (2005). Visco-elasto-capillary thinning and break-up of complex fluids. *Rheology Reviews*, *3*(05), 1–48.

McKinley, G. H., & Tripathi, A. (2000). How to extract the Newtonian viscosity from capillary breakup measurements in a filament rheometer. *Journal of Rheology*, *44*(3), 653–670. https://doi.org/10.1122/1.551105

Miller, E., Clasen, C., & Rothstein, J. P. (2009). The effect of step-stretch parameters on capillary breakup extensional rheology (CaBER) measurements. *Rheologica Acta*, *48*, 625–639. https://doi.org/10.1017/CBO9781107415324.004

Ober, T. J., Haward, S. J., Pipe, C. J., Soulages, J., & McKinley, G. H. (2013). Microfluidic extensional rheometry using a hyperbolic contraction geometry. *Rheologica Acta*, *52*(6), 529–546. https://doi.org/10.1007/s00397-013-0701-y

Papageorgiou, D. T. (1995). On the breakup of viscous liquid threads. *Physics of Fluids*, *7*(7), 1529–1544. https://doi.org/10.1063/1.868540

Rubinstein, M., & Colby, R. H. (2003). *Polymer Physics* (p. 458). p. 458. Oxford University Press.

Sachsenheimer, D., Hochstein, B., Buggisch, H., & Willenbacher, N. (2012). Determination of axial forces during the capillary breakup of liquid filaments - the tilted CaBER method. *Rheologica Acta*, *51*(10), 909–923. https://doi.org/10.1007/s00397-012-0649-3

Sachsenheimer, D., Hochstein, B., & Willenbacher, N. (2014). Experimental study on the capillary thinning of entangled polymer solutions. *Rheologica Acta*, *53*(9), 725–739. https://doi.org/10.1007/s00397-014-0789-8

Sankaran, A. K., Dros, D. A., Meerman, H. J., Picken, S. J., & Kreutzer, M. T. (2013). Increasing the stability of high contraction ratio flow of Boger fluids by pre-deformation. *Journal of Non-Newtonian Fluid Mechanics*, *196*, 27–35. https://doi.org/10.1016/j.jnnfm.2012.12.015

Schümmer, P., & Tebel, K. H. (1983). A new elongational rheometer for polymer solutions. *Journal of Non-Newtonian Fluid Mechanics*, *12*(3), 331–347. https://doi.org/10.1016/0377-0257(83)85006-X

Sousa, P. C., Vega, E. J., Sousa, R. G., Montanero, J. M., & Alves, M. A. (2017). Measurement of relaxation times in extensional flow of weakly viscoelastic polymer solutions. *Rheologica Acta*, *56*(1), 11–20. https://doi.org/10.1007/s00397-016-0980-1

Szabo, P. (1997). Transient filament stretching rheometer: Force balance analysis. *Rheologica Acta*, *284*, 277–284.

Szabo, P., McKinley, G. H., & Clasen, C. (2012). Constant force extensional rheometry of polymer solutions. *Journal of Non-Newtonian Fluid Mechanics*, *169–170*, 26–41. https://doi.org/10.1016/j.jnnfm.2011.11.003

Taylor, G. I. (1934). The Formation of Emulsions in Definable Fields of Flow. *Proceedings of the Royal Society of London*, *146*(858), 501–523.

Tirtaatmadja, V., McKinley, H. G., & Cooper-White, J. J. (2006). Drop formation and breakup of low viscosity elastic fluids: Effects of molecular weight and concentration. *Physics of Fluids*, *18*(4). https://doi.org/10.1063/1.2190469

Vadillo, D. C., Mathues, W., & Clasen, C. (2012). Microsecond relaxation processes in shear and extensional flows of weakly elastic polymer solutions. *Rheologica Acta*, *51*(8), 755–769. https://doi.org/10.1007/s00397-012-0640-z

Verbeke, K., Formenti, S., Vangosa, F. B., Mitrias, C., Reddy, N. K., Anderson, P. D., & Clasen, C. (2020). Liquid bridge length scale based nondimensional groups for mapping transitions between regimes in capillary break-up experiments. *Physical Review Fluids*, *5*(5), 1–8. https://doi.org/10.1103/PhysRevFluids.5.051901

Verhulst, K., Moldenaers, P., & Minale, M. (2007). Drop shape dynamics of a Newtonian drop in a non-Newtonian matrix during transient and steady shear flow. *Journal of Rheology*, *51*(2), 261–273. https://doi.org/10.1122/1.2426973